

Total internal reflection quasi phase matching based fourth harmonic generation in a parallel uniaxial crystal of magnesium oxide doped Lithium Niobate

JAYA SAHA*, SUMITA DEB

Department of Electrical Engineering, National Institute of Technology, Agartala, Barjala, Jirania, Tripura (west), Pin-799046, Tripura, India

This paper analytically describes fourth-harmonic generation by utilizing the phenomena of total internal reflection quasi-phase-matching in a parallel slab geometry of uniaxial crystal made of magnesium oxide doped Lithium Niobate. The effects of optical loss, namely, linear absorption, GH shift, and reflection loss on account of surface roughness, have been considered in this analysis. Finally, the analysis has also taken into account the cataclysmic effect that arises from the nonlinear law of reflection. The effects of variation of related slab parameters, i.e., length, thickness on the fourth harmonic efficiency, have also been studied. When compared to other approaches (e.g., Cascade, periodic polling) utilized for fourth-harmonic generation, this scheme greatly increased the conversion efficiency. The maximum conversion efficiency obtained for an operating wavelength of 750 nm is 2.05%.

(Received September 30, 2022; accepted October 9, 2023)

Keywords: Fourth harmonic generation, TIR-QPM, Parallel slab, Uniaxial crystal, MgO: LN

1. Introduction

Harmonic generation includes the generation of new wavelengths, which are multiples of fundamental wavelengths through nonlinear processes. Generally, this phenomenon is accomplished by the utilization of various nonlinear crystals. During fourth harmonic (FH) generation, a light with wavelength, which is $1/4^{\text{th}}$ of the fundamental wavelength, [1] is generated. It generally happens through two stages of cascaded nonlinear interaction [31]. The primary interaction is the second harmonic (SH) generation of fundamental wavelength, accompanied by using the additional SH generation of the generated wavelength. Cascaded FH generation is generally achieved by the utilization of two nonlinear crystals where every crystal is used for doubling the fundamental input wavelength [1,32]. Quadrature frequency conversion is the other alternative technique where two nonlinear crystals are utilized for each step of frequency conversion; therefore, four nonlinear crystals are required for FH generation [2]. Achieving phase-matching configuration becomes more complex due to the utilization of multiple crystals in the frequency conversion process. FH generation by a cascaded process in a single crystal is reported by Brett A. Hooper et al. [3] in LiNbO_3 , where conversion efficiency is 3.3×10^{-6} .

The effective fourth-order nonlinearity for FH generation in a single lithium formate crystal was first reported by Akhmanov et al. [4]. Xianfeng Chen et al. [5] also reported the quasi-phase match (QPM) based direct fourth-order harmonic generation in periodically poled LiNbO_3 crystal. Thus, materials with fourth-order optical

nonlinearity $\chi^{(4)}$ susceptibility can be used for fourth-order harmonic generation. In case of QPM based FH generation in a nonlinear optical material with periodic poling, the fabrication of crystals with high and consistently confirmed quality is difficult and possible only for certain crystal materials with fairly limited thickness.

In 1962, Armstrong et al. [6] were the first to suggest the idea of QPM by utilizing the technique of “Total Internal reflection (TIR)” in the geometry of a plane parallel plate. In TIR-QPM, the crystal is not domain inverted; rather the light waves are made to propagate in such a way that they are inverted in space. This eliminates error due to fabrication, and usually, the conversion efficiency increases effectively. This phenomenon has been reported by many researchers using different isotopic crystals like zinc sulfide (ZnS), zinc selenide (ZnSe), gallium arsenide (GaAs) in both non-resonant and resonant condition for obtaining second harmonic generation [7-9]. Resonant is that situation where the length between two consecutive bounces is equivalent to an odd multiple of coherence length (L_{coh}) [27]. Whereas in non-resonant condition, the distance between two immediate bounces is not matching with the odd multiple of coherence length, but it is also not matching with the even multiple of L_{coh} . Although non-resonant scenario provides less stringent condition, the resonant situation gives much higher conversion efficiency.

FH generation has been demonstrated analytically in this paper by the utilisation of TIR-QPM phenomenon in a parallel slab of anisotropic crystal. This anisotropic crystal slab is made of magnesium oxide (MgO) doped Lithium

Niobate (MgO: LN) material having an optic axis in the plane of incidence and parallel to the refracting edge. The MgO: LN crystal is used to reduce the photorefractive effect, and at the same time, it has a high damage threshold than Lithium Niobate [10]. This scheme seems much easier technologically than other approaches (e.g., Cascade, periodic polling) utilized for FH generation. After determining the efficiency of conversion under ideal condition, the impact of potentially limiting variables, that is, linear absorption, surface roughness, Goos – Hänchen (GH) shift, and finally the results have been analyzed considering the impact of the nonlinear law of reflection (NLR) to obtain a more realistic approach for the proposed FH generation scheme. The effect on the efficiency of resultant FH conversion for the variation in slab length, thickness has also been studied in this analysis.

2. Proposed scheme

The fourth-order harmonic generation has been proposed by the utilization of TIR-QPM phenomenon in the geometry of parallel slab made of MgO: LN. The schematic diagram is shown in Fig. 1, where the coupling of input and output occurs through the slanted ends of the slab. The analysis is performed by considering fundamental optical radiation of frequency ω having an incidence angle of ϕ_i with respect to normal at the slanted end of the slab. α is the angle between wavevector and optic axis.

Refraction angle ϕ_r is calculated from Snell's law of refraction, and it is given as $\phi_r = \sin^{-1}\left(\frac{\phi_i}{n}\right)$.

Here, n denotes the refractive index of the selected material (MgO: LN) for the corresponding fundamental and harmonic frequency, and it has been calculated from the standard Sellmeier Equation [13].

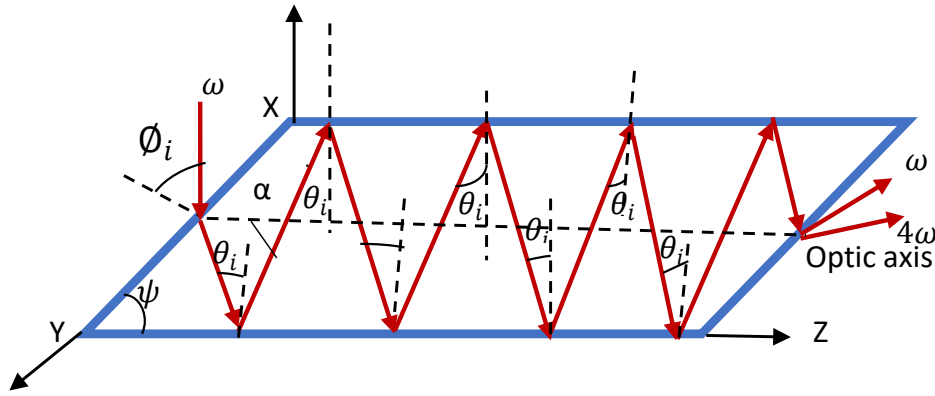


Fig. 1. The geometry of the parallel slab represents the fourth harmonic frequency conversion scheme (color online)

Therefore, the incidence angle θ_i at the bounce point inside the slab is given as

$$\theta_i = \frac{\pi}{2} - (\phi_r + \psi)$$

Here, ψ is the angle between the slanted end face and the horizontal plane of the slab. In order to ensure repeated TIR inside the slab θ_i must be greater than the respective critical angle for both fundamental and harmonic frequencies. Owing to the fact that the proposed slab has a parallel geometry, the geometrical path length between successive bounces and the incidence angle for both the fundamental and FH waves remain identical along the entire length of the slab L . This analysis has been performed for type-I polarization configuration where the waves of pump and FH beams have a p polarization and a s polarization, respectively.

$$p\alpha_s^{NL}(r, \omega_s) = \frac{q!}{2^{q-1}} \sum_{\alpha_1, \dots, \alpha_q} \varepsilon_0 \chi_{\alpha_1, \dots, \alpha_q}^q(-\omega_s; \omega_1, \dots, \omega_q) E_{\alpha_1}(r, \omega_1) \dots E_{\alpha_q}(r, \omega_q) \quad (2)$$

Factor $q!$ accounts for the intrinsic permutation symmetry of the nonlinear susceptibilities if all frequencies $\omega_1, \omega_2, \dots, \omega_s$ are nonzero and different. The

3. Mathematical analysis

When generating a higher-order harmonic by the fundamental Gaussian beam, the amplitude A_q of the frequency component $\omega_q = q\omega$ of the optical field must be followed by the equation [14, 15]

$$\nabla^2 A_q + 2ik_q \frac{dA_q}{dz} = -\frac{4\pi}{c^2} \omega_q^2 p_q^{NL} \exp(-i\Delta kz) \quad (1)$$

where wave vector mismatch between interacting waves is denoted by Δk , and it is equal to $k_q - qk_1$.

Now the nonlinear polarization p_q^{NL} , and its complex amplitude, is expressed as [14]

indices $\alpha_1, \alpha_2, \dots, \alpha_s$ are cartesian subscripts (x, y, or z). Equation (2) defines the q^{th} order nonlinear optical

susceptibility tensor $\chi^{(q)}$. Here, the susceptibility of q^{th} order harmonic is $\chi^{(q)}$, i.e., $\chi^{(q)}(q\omega = \omega + \omega + \dots)$.

The complex amplitude E_q of a higher-order harmonic in the plane wave limit can be given by [25]

$$\frac{dE_q}{dz} = \frac{i2\pi\omega_q}{n_q c} p_q^{NL} \exp(-i\Delta k L_b) \quad (3)$$

and

$$E_q = \frac{i2\pi\omega_q}{n_q c} p_q^{NL} J_q(\Delta k, z_0, L_b) \quad (4)$$

$$J_q(\Delta k, z_0, L_b) = \int_{z_0}^{L_b} e^{i\Delta k z} dz = \frac{e^{i\Delta k L_b} - e^{i\Delta k z_0}}{i\Delta k} \quad (5)$$

Here, $z=z_0$ represents the starting point of each bounce point.

$z=L_b$ represents the end point of each interaction length.

$$|J_q(\Delta k, z_0, L_b)|^2 = L_b^2 \text{sinc}^2\left(\frac{\Delta k L_b}{2}\right)$$

In our analysis $z_0 = 0$.

While neglecting the pump depletion, the amplitude of the 4th order harmonic field in a medium of length L_b is given by [14]

$$E_4 = -\frac{i2\pi\omega_4}{n_4 c} p_4^{NL} \text{sinc}\left(\frac{\Delta k L_b}{2}\right) e^{i\Delta k L_b/2}$$

$$E_4 = -\frac{i2\pi\omega_4}{n_4 c} p_4^{NL} \text{sinc}\left(\frac{\Delta k t}{2\cos\theta_i}\right) e^{i\frac{\Delta k t}{2\cos\theta_i}} \quad (6)$$

where c represents the velocity of light and n_4 denotes the refractive of material at a wavelength of λ_4 . L_b is the geometric path length between two consecutive bounces, and it is an odd integer multiple of coherence length (L_{coh}). $L_b = (2g + 1)L_{\text{coh}} = \frac{t}{\cos\theta_i}$ Here g is an integer and $L_{\text{coh}} = \frac{\pi}{\Delta k}$. Wave vector $k_m = \frac{n_m \omega_m}{c}$ ($m=1,4$) and Δk is the wavevector mismatch between interacting waves, and it is equal to $(k_4 - 4k_1)$. Three-phase shift contributes to the global phase shift $\Delta\phi$ between any two successive bounces. So, $\Delta\phi = \Delta k L_b + \Delta\phi_F + \epsilon \cdot \pi$. Here, $\Delta k L_b$ denotes the mismatch in phase among the waves that are interacting with one another during dispersion, $\Delta\phi_F = \text{Relative Fresnel phase shifts} = \phi_4 - 4\phi_1$. During the conditions of TIR, at angles of incidence θ_i above the critical angle θ_{cri} , the Fresnel phase shifts for p and s polarized light are given by [9]

$$\tan(\phi_p/2) = N'(N'^2 \sin^2 \theta_i - 1)^{1/2} / \cos \theta_i$$

$$\tan(\phi_s/2) = (N'^2 \sin^2 \theta_i - 1)^{1/2} / (N' \cos \theta_i)$$

where, $N' = N_0/N_1$ is the high to low ratio of refractive indices of the media of incidence and refraction

respectively ($N' > 1$) and additional phase shift $\delta\phi = \epsilon\pi$ ($\epsilon = 1$ if $\chi_{\text{eff}}^{(4)}$ changes sign, $\epsilon = 0$ if not).

$\delta\phi = \pi$ for ppppp polarization
 $\delta\phi = \pi$ for pssss polarization
 $\delta\phi = \pi$ for ssssp polarization
 $\delta\phi = \pi$ for sppps polarization
 $\delta\phi = 0$ for sssss polarization
 $\delta\phi = 0$ for pppps polarization
 $\delta\phi = 0$ for psssp polarization
 $\delta\phi = 0$ for spppp polarization

The approximate relationship between the susceptibility tensor of higher-order $\chi^{(q)}$ and lower-order

$\chi^{(p-1)}$ has been used [5]. It is given by $\frac{\chi^{(q)}}{\chi^{(q-1)}} = \frac{1}{E_0}$ [5].

Here the magnitude of the electric field, on average, found inside an atom is E_0 . So, the relationship between the effective susceptibility tensor of fourth-order and second-order $\chi_{\text{eff}}^{(2)}$ is given by

$$\frac{\chi^{(q)}}{\chi^{(q-2)}} = \frac{1}{E_0^2}$$

Here, the optic axis is not parallel to the propagation vector of generated harmonic. Therefore, there is a propagation of the component wave (p and s) of the generated harmonic field E_4 resulting in an additional phase shift of the component wave during consecutive bounces. Now, the Jones Vector concept has been used to determine the component of wave E_4 (p and s) in terms of Rotation Matrix $R(\alpha)$ [26] as follows,

$$R(\alpha) = \begin{bmatrix} \cos\alpha & \sin\alpha \\ -\sin\alpha & \cos\alpha \end{bmatrix}$$

For TIRQPM

$$\begin{bmatrix} E_{4p} \\ E_{4s} \end{bmatrix} = \begin{bmatrix} \cos\alpha & \sin\alpha \\ -\sin\alpha & \cos\alpha \end{bmatrix} \begin{bmatrix} 0 \\ 1 \end{bmatrix} = \begin{bmatrix} \sin\alpha \\ \cos\alpha \end{bmatrix} \quad (7)$$

For a wave with a linear polarization, the electric vector is represented by jones vector $\rho_{y=0} = \begin{bmatrix} 0 \\ 1 \end{bmatrix}$ which works in execution of a zero-phase, unit-amplitude, oscillation of harmonic along the y -axis [26].

The effect of TIR has been incorporated for generating fourth-order harmonic. The harmonic electric field for any intermediate length L_j ($j > 1$) for s and L_{j-1} ($j > 0$) p wave can be written as [30],

$$E_{4S(TIRQPM)}(L_j) = \{ e^{-i\Delta\phi_1} \cos\alpha + e^{-i\Delta\phi_2} \cos^2\alpha + \dots + e^{-i(j-1)\Delta\phi_{(j-1)}} \cos^{(j-1)}\alpha \} E_{4S}(L_1) \quad (8)$$

$$E_{4P(TIRQPM)}(L_{j-1}) = \{e^{-i\Delta\theta_1} \sin\alpha + e^{-i\Delta\theta_2} \sin^2\alpha + \dots + e^{-i(j-1)\Delta\theta} \sin^{(j-1)}\alpha\} E_{4P}(L_1) \quad (9)$$

L_j is the j^{th} bounce length. Where, $j=1, 2, \dots, n$ = No of bounce

The net FH electric field for n number of bounces is given by

$$E_4(L_1 + L_2 + \dots + L_n) = \sum_{j=1}^n \{E_{4S(TIRQPM)}(L_j) + E_{4P(TIRQPM)}(L_{j-1})\} \quad (10)$$

The time-average FH intensity I_4 can be expressed as

$$I_4 = \frac{n_4 c}{8\pi} E_4 E_4^* \quad (11)$$

Finally, FH conversion efficiency has been expressed as

$$\eta_{con} = \frac{I_4}{I_1} \times 100\% \quad (12)$$

where, I_1 is the fundamental input intensity.

4. Factors limiting the conversion yield

The conversion efficiency of the TIR-QPM technique is limited by certain important factors related to the material parameters, fabrication technique, beam properties, etc. These factors include surface roughness, Goos-Hänchen shift, absorption, and diffraction due to NLR. The effects of these factors have to be considered in calculating the efficiency of the generated fourth harmonic radiation.

4.1. Surface roughness

Whenever a light beam hits any rough surface, scattering will occur at the point of reflection. For this reason, there will be a reduction in the amount of reflected light. Strehl Ratio is used for measuring the drop [9]. Equation (13) represents the coefficient of reflection that can be expressed in terms of incident angle and wavelength.

$$r = \exp\left[(-\sigma \frac{4\pi n}{\lambda} \cos\theta_i)^2\right] \approx 1 - (\sigma \frac{4\pi n}{\lambda} \cos\theta_i)^2 \quad (13)$$

where, $\sigma = \frac{\gamma}{12}$ P-V value/12. Here, the P-V value represents the peak to valley value of the surface to be considered, and in this analysis, 6 nm has been considered for MgO: LN to incorporate the effect of reflection loss [17].

The fundamental incident intensity at each point is multiplied by its corresponding reflection coefficient in order to determine the reflected intensity propagating in the next path after allowing for the reflection loss at that bounce point. Similarly, the effect of reflection loss on the generated FH (calculated with the reflected fundamental value at the corresponding bounce point) is considered in the analysis.

4.2. GH shift

When a collimated beam of light travels across two dielectric mediums, its total internal reflection experiences a longitudinal shift of [16]

$$S^E = \left(\frac{2}{k_i}\right) \frac{\tan\theta_{cri}}{(\sin^2\theta_i - \sin^2\theta_{cri})^{1/2}} \quad (14)$$

$$k_i = 2\pi n_i / \lambda_i$$

Here, k_i is the wave vector corresponding to the vacuum wavelength λ_i , n_i is the refractive index of media with a higher density. The incidence angle is denoted by θ_i while the critical angle is denoted by θ_{cri} .

The useable length of the crystal is reduced due to this longitudinal shift. Upper and lower surface GH shifts have been calculated; for MgO:LN, the fundamental input wavelength of 3000 nm has experienced a total GH phase shift of 1.8 μm for the length of the slab of 8 mm.

4.3. Absorption

The frequency conversion procedures are negatively impacted by linear absorption, which also drastically reduces the efficiency of the frequency conversion. [28]. Linear absorption coefficients α_ω and $\alpha_{4\omega}$ are wavelength dependent and are usually less than 1. In general, absorption of fundamental cannot be completely eradicated, although it is often masked by scattering at very low absorption. Absorption has another harmful effect on material heating. Drift in phase matching conditions can be produced due to absorption, thereby reducing the conversion efficiency.

In this analysis linear absorption coefficient of $\alpha_\omega = 0.02 \text{ cm}^{-1}$ and $\alpha_{4\omega} = 0.002 \text{ cm}^{-1}$ have been considered [19].

4.4. Diffraction due to NLR

M. Raybaut has pointed out the NLR noted by Pershan and Bloembergen [11] as the basic reason for the drop in conversion gain of the parametric oscillations in a plane parallel plate [12]. According to this law, when a light beam is reflected on a nonlinear medium for FH generation, besides the generated collinear field in the medium, another "homogeneous" FH field also gets generated, which satisfies Snell-Descartes law:

$$n_{\omega} \sin \theta_{\omega} = n_{4\omega} \sin \theta_{4\omega} \quad (15)$$

The above equation depicts that the fundamental angle of incidence (θ_{ω}) and the generated FH, due to optical dispersion, angle of incidence ($\theta_{4\omega}$) are not equivalent and must satisfy Snell-Descartes law so that the generated FH wave can be a plane wave. The homogeneous radiated FH wave is collinear with the reflected FH wave at the

boundary interface, thus preserving the plane wave propagation [29]. The angle variation between the colinear and the homogeneous FH wave is given as [11]:

$$\delta\theta \approx -\left(\frac{\delta n}{n}\right) \tan \theta_{\omega} \quad (16)$$

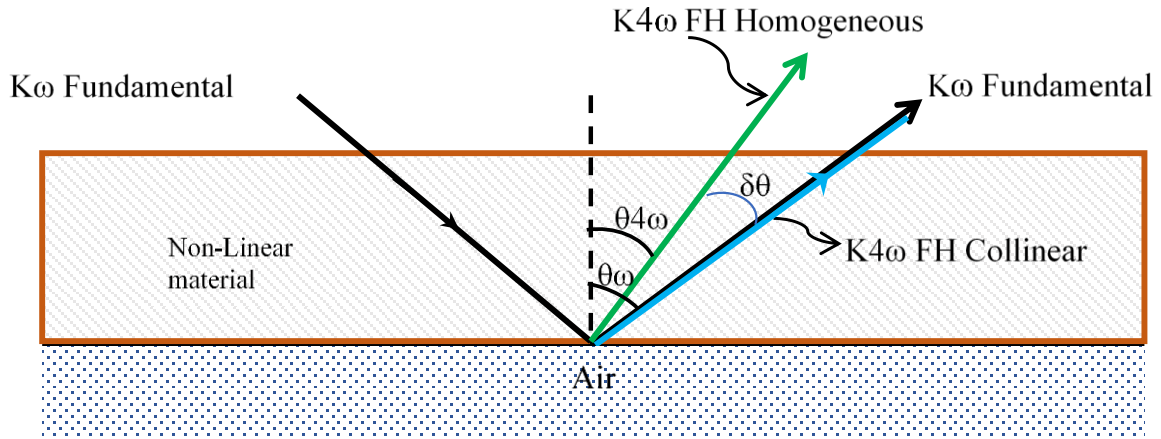


Fig. 2. FH wave collinear to fundamental wave and generated Homogeneous wave due to nonlinear law of reflection (color online)

Here, $\delta n = n_{4\omega} - n_{\omega}$ is the optical dispersion, and $n \approx n_{4\omega} \approx n_{\omega}$.

At each bounce point, two FH waves are generated, which depends upon incidence angle and optical dispersion, separating each wave. The angle of separation increases as both waves propagate, creating a spatial walk-off, which reduces the overlapping conditions between the interacting waves. Depending upon slab length, after some TIR bounces inside the slab, the fundamental and FH wave interact with each other, which results in destructive interference, thereby reducing the efficiency of the output wave. The number of bounces after which recombination occurs is given as

$$N_{rec} \approx 2|\tan \theta_{\omega} / \delta\theta| \approx 2|n / \delta n| \quad (17)$$

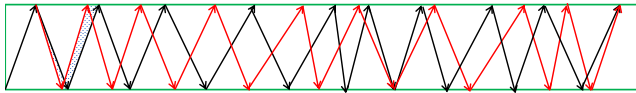


Fig. 3. The pump and FH waves tending towards recombination with increasing number of bounces (color online)

The two FH fields propagate along with the fundamental optical field throughout the slab. It is observed that after a certain number of bounces, the spatial walk-off between these two fields increases to such an extent that destructive interference scenario results, resulting in decreased generated output. Now again (Fig. 3) after a certain number of bounces, there is a chance of

increase in interference between collinear and “homogeneous” FH waves resulting in constructive interference. Hence the conversion efficiency rises. As a result, the recombination of collinear and homogeneous FH fields alternately repeats the generation of both constructive and destructive FH fields after certain TIR bounces.

5. Simulation results and discussions

The computer-aided simulation for the parallel slab configuration of magnesium oxide doped LiNbO₃ crystal has been performed in the MATLAB platform. The temperature-dependent Sellmeier equation has been used to measure the refractive index of 5 mol% MgO doped lithium niobate (MgO: LN) [13]. In the present analysis, a beam waist of 100 μm and input intensity of 7 Mw/cm^2 for the fundamental beam has been considered with adequate consideration given to the damage threshold value of the material [10]. In order to maximize output efficiency, tests were performed to see what would happen if the slab parameters were changed.

Fig. 4 shows the variation in coherence length of MgO: LN at different wavelengths. Therefore, from Fig. 4, it can be said that comparatively, lower-order TIR-QPM is possible at a wavelength from (2.36 to 3.48) μm however, higher-order TIR-QPM is possible at wavelengths from (2 to 2.35) μm and (3.49 to 4) μm .

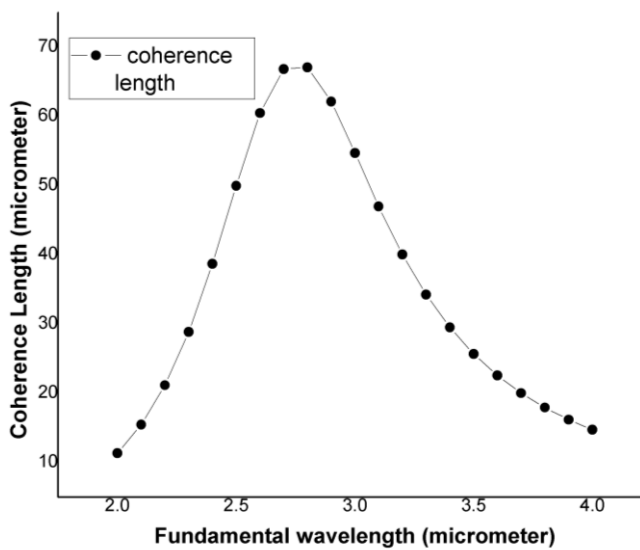


Fig. 4. Variation in coherence length of MgO: LN with respect to different input wavelength at a temperature of 298 K

5.1. Effect of variation in slab length

In a parallel slab, during the collimated beam's propagation within the plate, the length between the consecutive bounce and the incidence angle is fixed at each bounce point. By carefully selecting the angle of incidence, it has ensured that the distance between each pair of successive bounces is an odd-integer multiple of the coherence length for the wavelength of the input that is being taken into account. Additionally, the requirement for constructive interference has been satisfied. The number of TIR bounces in parallel slab geometry increases with increasing slab length. This eventually increased the efficiency of conversion with the increment in length of the slab in both ideal and lossy conditions, i.e., after the inclusion of limiting factors. But after the inclusion of the NLR, it is observed that conversion efficiency has been trimmed down after a certain number of TIR bounce points. Due to the NLR at each bounce point, two FH waves are generated. The angle of separation increases as both waves propagate, creating a spatial walk-off, which reduces the overlapping conditions between the interacting waves.

The produced collinear FH field experiences a phase shift of 0 or 2π at each bounce point, but the homogeneous FH field undergoes dissimilar phase shifts after each bounce point. Therefore, effective constructive, as well as a destructive FH field, are generated at different TIR bounces due to recombination of both collinear and homogeneous FH fields. Fig. 5 shows the variation in the total phase shift of the resultant FH field with respect to the number of bounces for generating 750 nm wavelength where the number of TIR bounce increases from 10 to 40 with the increase of slab length from 4 mm to 7 mm. From Fig. 5, it is observed that the net total phase shift for the resultant FH field is approximately 0 at 20 and 40 number bounce points. Therefore, constructive interference occurred at 20 and 40 number bounce points. The variation

in the efficiency of conversion as a function of slab length and the number of TIR bounces has been shown in Figs. 6 and 7, where NLR, as well as limiting factors, are considered for generating 750 nm wavelength. Therefore, from Fig. 6 and Fig. 7, it is observed that destructive interference occurred at 43rd and 51st bounce points, i.e., at the slab length of 5.3 mm and 6.3 mm, respectively, and the maximum efficiency of 2.05234% is obtained at the 45th bounce point, i.e., at the slab length of 5.5 mm.

$\Lambda = 3 \mu\text{m}$, temperature = 298 K, $\phi_i = 0.73759$ radian,
 $t = 140 \mu\text{m}$, $\psi = 0.3$ radian, $x = 100 \mu\text{m}$

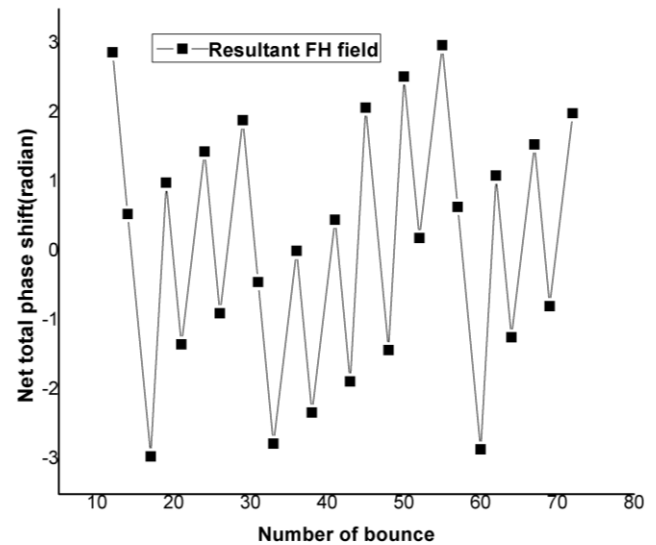


Fig. 5. Variation in total phase shift as a function of number of bounces for generating 750 nm wavelength

$\Lambda = 3 \mu\text{m}$, temperature = 298 K, $\phi_i = 0.73759$ radian,
 $t = 140 \mu\text{m}$, $\psi = 0.3$ radian, $x = 100 \mu\text{m}$

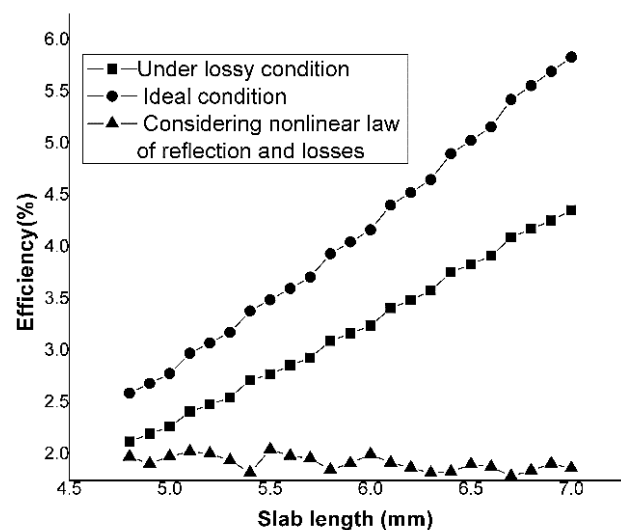


Fig. 6. Variation in efficiency with respect to slab length for generating 750 nm wavelength

$\Lambda = 3 \mu\text{m}$, temperature = 298 K, $\phi_i = 0.73759$ radian,
 $t = 140 \mu\text{m}$, $\psi = 0.3$ radian, $x = 100 \mu\text{m}$

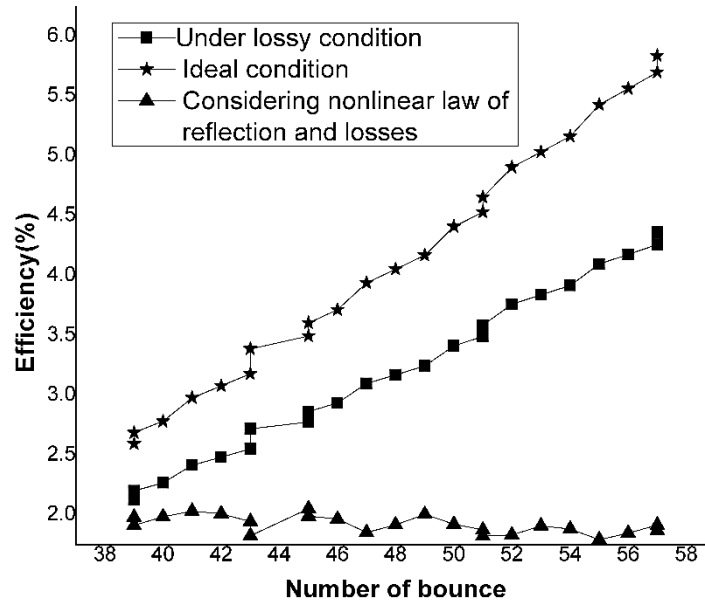


Fig. 7. Variation in efficiency with respect to number of bounce point for generating 750 nm wavelength

Table 1. Effect of variance in slab length (L). $t=140 \mu\text{m}$, $\psi=0.3$ rad, $I=7 \text{ Mw/cm}^2$, temperature=298 K, $x=100 \mu\text{m}$

Input wavelength (nm)	Output wavelength (nm)	ϕ_i (radian)	Slab length (mm)	Efficiency (%)		
				Ideal condition	Lossy condition	With nonlinear reflection
3000	750	0.73759	5	2.78415	2.26906	1.98532
			5.5	3.49675	2.77786	2.05234
			6	4.17209	3.17261	1.91763
			6.5	5.03531	3.83976	1.90944
			7	5.83977	4.36303	1.87008
2200	550	0.56859	5.1	1.37482	1.16399	0.85165
			6	2.01462	1.65391	0.62161
			6.5	2.38022	1.91824	0.6667
			6.7	2.57445	2.06201	0.68984
			7	2.77629	2.21001	0.70788
2128	532	0.60442	4.5	0.82815	0.70272	0.48126
			5	1.0224	0.85062	0.58912
			5.5	1.29398	1.05556	0.66637
			6	1.53424	1.22713	0.49262
			6.5	1.86333	1.46126	0.53206

Table 2. Effect of variation in thickness (t). $L = 8 \text{ mm}$, $\psi = 0.3 \text{ rad}$, $I = 7 \text{ Mw/cm}^2$, temperature = 298 K, $x = 100 \mu\text{m}$

Input wavelength (nm)	Output wavelength (nm)	φ_i (radian)	Slab thickness (μm)	Number of bounces	Efficiency (%)		
					Ideal condition	Lossy condition	With nonlinear reflection
3000	750	0.652	141	37	5.37152	4.792	1.972
		0.634	143	36	4.553886	3.99	1.412
		0.627	145	35	3.9608	3.485	1.012
		0.613	147	34	3.44538	3.112	0.935
		0.619	149	33	3.16968	2.823	0.885
2200	550	0.877	141	44	2.1608	1.994	0.843
		0.882	143	43	2.0334	1.9864	0.80466
		0.924	145	42	1.76231	1.5695	0.67155
		0.958	147	41	1.68511	1.634	0.4999
2128	532	1.0882	149	40	1.26254	1.12	0.373
		1.137	141	50	1.67949	1.358	0.659
		1.111	143	49	1.56077	1.285	0.62194
		1.121	145	48	1.31786	1.112	0.47887
		1.165	147	47	1.1233	1.096	0.23085
		1.273	149	46	1.10253	0.98448	0.118

The impact of increasing the length of the slab for generating 532 nm and 550 nm wavelength are shown in Figs. 9, 10, 11, and 12. From Fig. 9 and 10, it is observed that constructive interference occurred at the 28th bounce point, i.e., at the slab length of 5 mm, and the maximum efficiency at that bounce point is 0.58912% for generating 532 nm wavelength when NLR as well as limiting factors, are considered. In the same way from Figs. 10 and 11, it is

observed that maximum efficiency of 0.85165 % is obtained for generating 550 nm wavelength at 27th bounce point, i.e., at slab length of 5.1 mm. Fig. 8 illustrates the variation of conversion efficiency in terms of the net total phase shift and the highest possible conversion efficiency occurs when the net total phase shift is zero. Therefore, constructive interference occurred at this point.

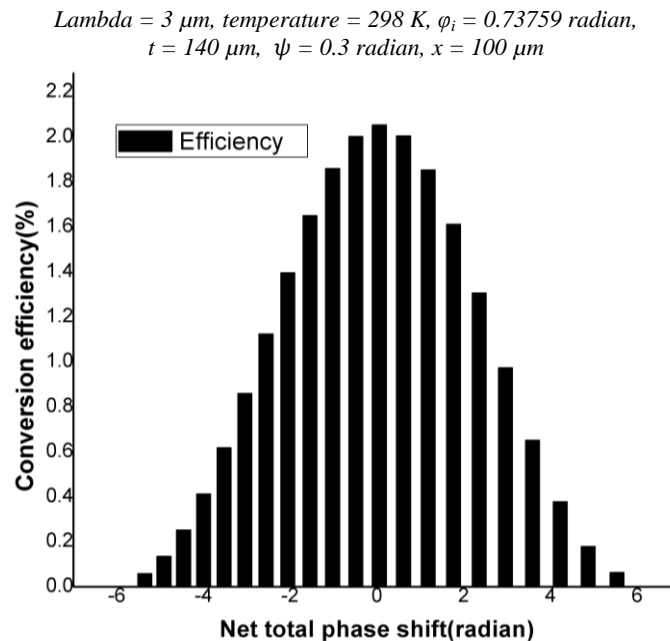


Fig. 8. Variation in efficiency with respect to net total phase shift for generating the wavelength of 750 nm during the consideration of nonlinear law of reflection and limiting factors

$\lambda = 2.128 \mu\text{m}$, temperature = 298 K, $\phi_i = 0.60442$ radian,
 $t = 140 \mu\text{m}$, $\psi = 0.3$ radian, $x = 100 \mu\text{m}$

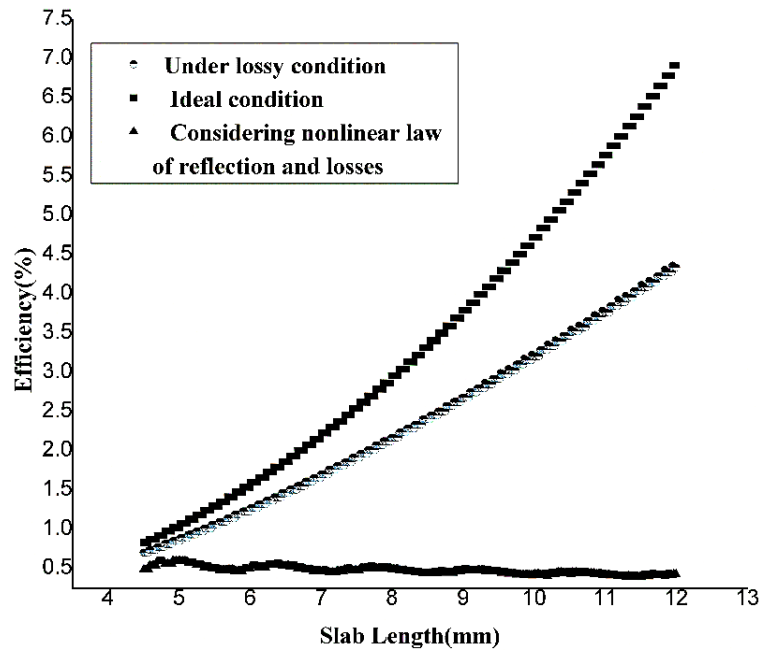


Fig. 9. Variation in efficiency as a function of slab length for generating 532 nm wavelength

$\lambda = 2.128 \mu\text{m}$, temperature = 298 K, $\phi_i = 0.60442$ radian,
 $t = 140 \mu\text{m}$, $\psi = 0.3$ radian, $x = 100 \mu\text{m}$

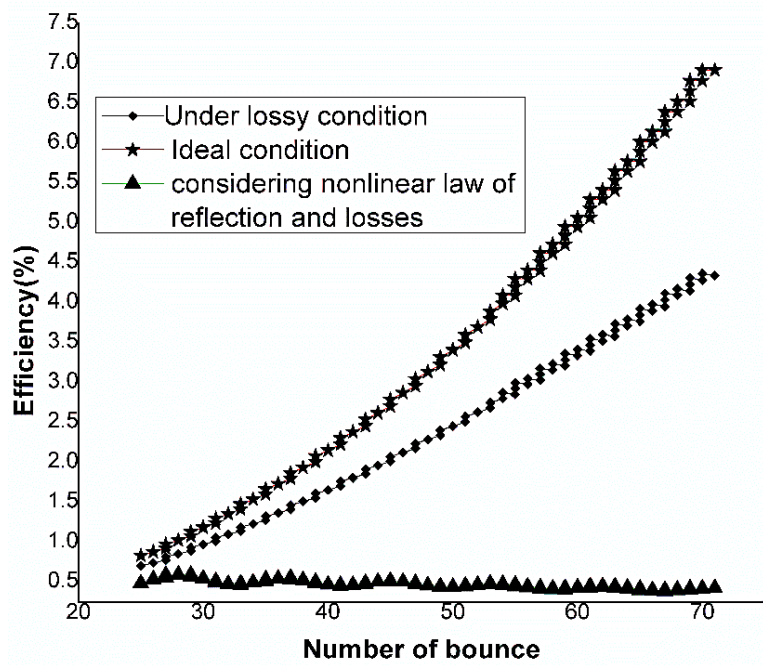


Fig. 10. Variation in efficiency with respect to number of bounces for generating 532 nm wavelength

$\lambda = 2.2 \mu\text{m}$, temperature = 298 K, $\phi_i = 0.56859$ radian,
 $t = 140 \mu\text{m}$, $\psi = 0.3$ radian, $x = 100 \mu\text{m}$

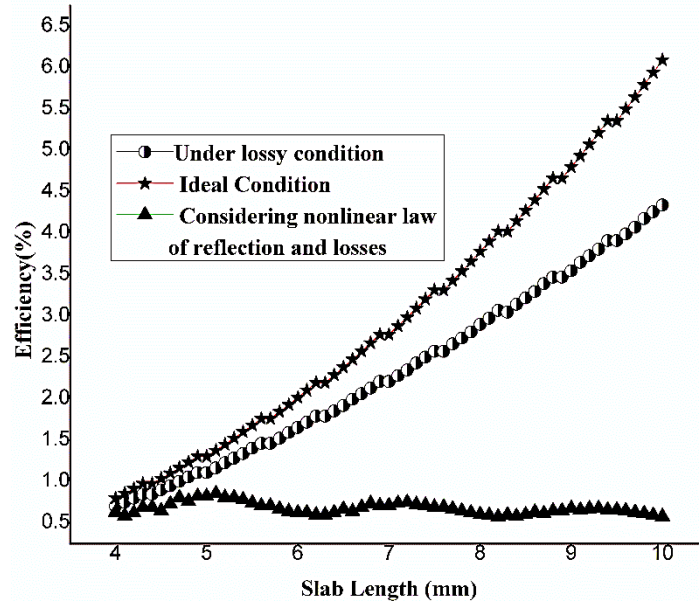


Fig. 11. Variation in efficiency with respect to slab length for generating 550 nm wavelength

$\lambda = 2.2 \mu\text{m}$, temperature = 298 K, $\phi_i = 0.56859$ radian,
 $t = 140 \mu\text{m}$, $\Psi = 0.3$ radian, $x = 100 \mu\text{m}$

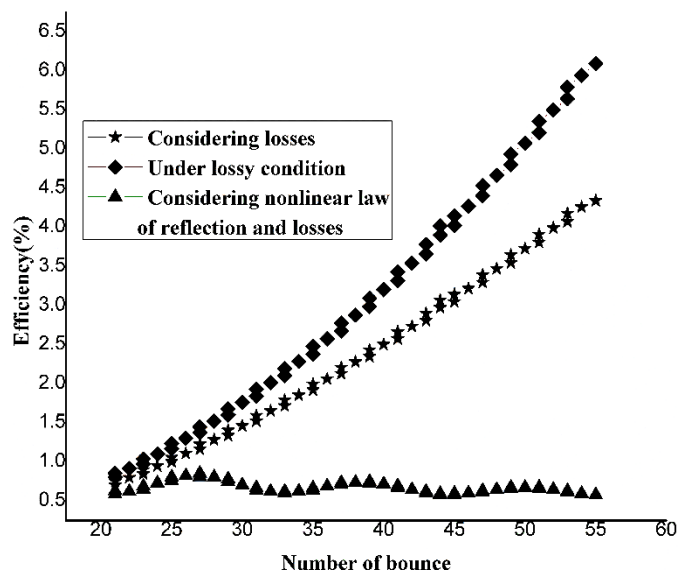


Fig. 12. Variation in efficiency as a function of number of bounces for generating 550 nm wavelength

5.2. Effect of variation in slab thickness

When the thickness of the slab has been varied from 141 to 149 μm in steps of 2 μm , the efficiency under ideal, lossy, and on consideration of NLR condition decreases with the increment in thickness of the slab. The decrease in conversion efficiency is due to the decrease in the number of bounces with the increase in the thickness of the slab. The angle of incidence has been set for the

incidence angle during thickness variation is also selected in such a way that the order of QPM for different application wavelengths of 532 nm, 550 nm, and 750 nm is fixed at 11, 9, and 3, respectively, and the maximum efficiency obtained at these wavelengths are 0.659%, 0.85165%, and 1.972% respectively. Table 2 demonstrates how thickness variation influences the performance parameter. Thickness modification in such a way that the geometric path length between two consecutive bounce sites is equivalent to an odd integer multiple of the

coherence length for the input wavelength that is being considered. In addition to this, the requirement for constructive interference has also been met.

6. Conclusion

In this paper, the FH generation using the phenomena related to TIR-QPM in a parallel slab geometry of anisotropic material (MgO: LN) has been described. The effects of several optical losses due to linear absorption, GH shift, and reflection loss on account of surface roughness, along with the effect arising from NLR, have been considered in this analysis. The effect of variation of slab parameters such as length and thickness on the FH efficiency is also being included in this study. The effect of NLR in FH generation using the TIR-QPM scheme has trimmed down the conversion efficiency as same as reported by M. Raybaut [11] during the second harmonic generation in parallel slab geometry of isotopic semiconductor. The proposed scheme demonstrates the technologically simple idea of QPM by utilizing TIR phenomena in the geometry of a parallel plate. This scheme has several advantages over the conventional methods, such as cascaded FH generation and quadrature frequency conversion methods that demand the utilization of multiple crystals for the conversion process. TIR-QPM method provides better efficiency as compared to conventional cascaded FH generation in a single crystal. The cascaded FH generation process in a single crystal is reported by Brett A. Hooper et al. [3] in LiNbO₃, where efficiency of conversion is significantly lower than our suggested frequency conversion approach.

FH generation by using the TIR-QPM scheme is shown by doing the simulation using different application wavelengths (like 532 nm, 550 nm, and 750 nm). The maximum conversion efficiency obtained for application wavelengths of 532 nm, 550 nm, and 750 nm is 0.66637%, 0.85165%, and 2.05234%, respectively, with due consideration for limiting factors as well as NLR. This proposed scheme significantly improved the convention efficiency as compared to the other conventional process.

From the application point of view, FH generation using MgO: LN material for generating 532 nm wavelength can be useful in fluorescence spectroscopy, optical alignment, green light illumination, and in some medical applications like treating vascular skin lesions, [21] endoscopy [22]. Also, 550 nm can be used in ozone monitoring instruments, [24] flow cytometry, [23] and 750 nm in near-infrared spectroscopy, [20] photodynamic therapy, and other medical applications requiring a large tissue penetration depth [22].

References

- [1] <https://www.rp-photonics.com/index.html>
- [2] D. Eimerl, IEEE Journal of Quantum Electronics **23**, 1361 (1987).
- [3] B. A. Hooper, D. J. Gauthier, J. M. J. Madey, Appl. Opt. **33**, 6980 (1994).
- [4] S. Akhmanov, A. Dubovik, S. Saltiel, I. Tomov, V. Tunkin, Soviet Journal of Experimental and Theoretical Physics Letters **20**, 117 (1974).
- [5] X. Chen, Y. Chen, Y. Xia, Appl. Opt. **44**, 1028 (2005).
- [6] J. A. Armstrong, N. Bloembergen, J. Ducuing, P. S. Pershan, Phys. Rev. **127**, 1918 (1962).
- [7] G. D. Boyd, C. K. N. Patel, Applied Physics Letters **8**, 313 (1966).
- [8] H. Komine, W. H. Long, J. W. Tully, E. A. Stappaerts, Optics Letters **23**, 661 (1988).
- [9] R. Haïdar, N. Forget, P. Kupecek, E. Rosencher, JOSA B **21**, 1522 (2004).
- [10] G. Li, Y. Cui, J. Wang, Optics Express **21**, 21790 (2013).
- [11] M. Raybaut, A. Godard, A. Toulouse, C. Lubin, E. Rosencher, Appl. Phys. Lett. **92**, 121112 (2008).
- [12] M. Raybaut, A. Godard, A. Toulouse, C. Lubin, E. Rosencher, Optics Express **16**, 18457 (2008).
- [13] Y. Jian-Quan, Y. Yi-Zhong, W. Peng, W. Tao, Z. Bai-Gang, D. Xin, C. Jin, H. J. Peng, H. S. Kwok, Chinese Physics Letters **18**, 1214 (2001).
- [14] J. Reintjes, Nonlinear optical parametric processes in liquids and gases, Elsevier, 2012.
- [15] R. W. Boyd, Nonlinear Optics, Academic Press, 2003.
- [16] A. W. Snyder, J. D. Love, Applied Optics **15**, 236 (1976).
- [17] Zhenyu Zhang, Bo Wang, Nianmin Zhang, Chaoge Xu, "High-efficiency super-smooth chemical mechanical polishing method for lithium niobate crystal" Publication of CN103978406A, China. Application CN201410197096.5A, Application publication date: 2014/08/13.
- [18] A. V. Smith, D. J. Armstrong, W. J. Alford, JOSA B **15**, 122 (1988).
- [19] J. R. Schwesyg, A. Markosyan, M. Falk, M. C. C. Kajiyama, D. H. Jundt, K. Buse, M. M. Fejer, Advances in Optical Materials, OSA Technical Digest (CD) (Optica Publishing Group), paper AIThE3 (2011).
- [20] G. R. Hunt, R. C. Evarts, Geophysics **46**, 316 (1981).
- [21] <https://integratedoptics.com/cw-lasers/532-nm-lasers/532-nm-laser-dpss-sm-fiber>.
- [22] <https://www.laserdiodesource.com/laser-diode-product-page/750nm-800mW-HHL-c-mount-LDX-Optronics#:~:text=Description%3A,a%20large%20tissue%20penetration%20depth>.
- [23] W. G. Telford, S. A. Babin, S. V. Khorev, S. H. Rowe, Cytometry Part A: The Journal of the International Society for Advancement of Cytometry **75**, 1031 (2009).
- [24] M. Dobber, R. Voors, R. Dirksen, Q. Kleipool, P. Levelt, Solar Physics **249**, 281 (2008).
- [25] C. R. Vidal, Fundamentals of Laser Interactions Springer, 221–7, 1985.
- [26] R. M. A. Azzam, N. M. Bashara, Ellipsometry and Polarized Light, North Holland, 1977.
- [27] A. Saha, S. Deb, Jpn. J. Appl. Phys. **50**, 102201

- (2011).
- [28] A. Saha, S. Deb, Optics Communications **284**, 4714 (2011).
- [29] S. Deb, A. Saha, Optik - International Journal for Light and Electron Optics **126**, 3371 (2015).
- [30] Moumita Saha, Sumita Deb, Pritam Kumar Mandal, Bhaswati Medhi, Ardhendu Saha, Opt. Eng. **60**(6), 066104 (2021).
- [31] Z. Ge, Z. Zhou, Y. Li, C. Yang, S. Liu, B.-S. Shi, Optics Letters **46**(2), 158 (2021).
- [32] K. Stoll, J.-J. Zondy, O. Acef, Opt. Lett. **22**(17), 1302 (1997).

*Corresponding author: jayasaha2013@gmail.com